

Crystallization kinetics of amorphous alumina–zirconia–silica ceramics

T. Chráska^{a,*}, J. Hostomský^b, M. Klementová^b, J. Dubský^a

^a Institute of Plasma Physics AS CR v.v.i., Za Slovankou 3, 18200 Prague, Czech Republic

^b Institute of Inorganic Chemistry AS CR v.v.i., Husinec-Řež 1001, 25068 Řež, Czech Republic

Received 12 February 2009; received in revised form 7 May 2009; accepted 13 May 2009

Available online 12 June 2009

Abstract

Crystallization kinetics of amorphous alumina–zirconia–silica ceramics was studied by nonisothermal differential scanning calorimetry (DSC). Different amorphous materials were produced by plasma spraying of near-eutectic Al_2O_3 – ZrO_2 – SiO_2 mixtures. Phase composition and microstructure of the amorphous materials and nanocrystalline products were analyzed. All of the investigated materials show an exothermic peak between 940 and 990 °C in the DSC experiments. The activation energies calculated from DSC traces decrease with increasing SiO_2 concentration. Values of the Avrami coefficients together with results of the microstructural observations indicate that tetragonal zirconia crystallization from materials containing more than 10 wt.% SiO_2 proceeds by a diffusion-controlled mechanism with nucleation occurring predominantly at the beginning of the process. In contrast, material with almost no SiO_2 exhibited a value of the Avrami exponent consistent with the crystal growth governed by processes at the phase boundary.

© 2009 Elsevier Ltd. All rights reserved.

Keywords: Nanocomposites; Al_2O_3 ; ZrO_2 ; SiO_2 ; Solid-state reaction

1. Introduction

Ceramic nanocrystalline powders can be conventionally synthesized in large quantities but the consolidation of nanopowders into mesoscopic structures and large bulk parts remains a challenge.¹ The powder consolidation process must allow retention of the nanometer grain size and at the same time bring residual porosity levels to a minimum. Moderate success has been achieved for certain ceramic materials by so-called Transformation Assisted Consolidation² or by Spark Plasma Sintering.³ Another approach uses thermal spraying to prepare nanostructured coatings by spraying agglomerated nanocrystalline feedstock while ensuring its only partial melting. The question remains whether some moderate gain in coating performance justifies economically the use of more expensive nanostructured feedstock.⁴ The deposits sprayed using solutions and suspensions are still in the early research and development phase.⁴ In an alternative approach, suitable materials are processed by rapid solidification technique to produce amorphous parts. The formation of nanostructured materials can then be achieved by appropriate heat treatment

to introduce nanocrystallites in the bulk. Such treatment has commonly been used for metallic glasses (e.g. Ref. 5) but is less common in the case of ceramics.

It has been previously reported that ceramic materials with near-eutectic composition can solidify as fully or partially amorphous solids due to rapid solidification (e.g. Refs. 6–10). In this work, the ternary Al_2O_3 – ZrO_2 – SiO_2 system was chosen as it contains binary and ternary eutectic points, alumina–zirconia is a well-studied system, and silica is a glass former. Nanocomposites comprising ZrO_2 nanocrystallites with average crystallite size as low as 12 nm embedded in fine amorphous matrix have been prepared by solid-state crystallization during heat treatment of plasma-sprayed amorphous parts.¹¹ In order to obtain an optimized nanocomposite product, it is necessary to understand and at least qualitatively describe the kinetics of demixing and crystallization and to determine the influence of individual chemical constituents on the underlying diffusion processes.

2. Experimental

Seven different material compositions (labeled as NZ, Eucor-A, Eucor-B, etc.) are shown in a partial ternary phase diagram (Fig. 1) and their composition is given in Table 1. The NZ material is commercially available as fused and crushed powder.

* Corresponding author. Tel.: +420 266 053 307; fax: +420 286 586 389.
E-mail address: tchraska@ipp.cas.cz (T. Chráska).

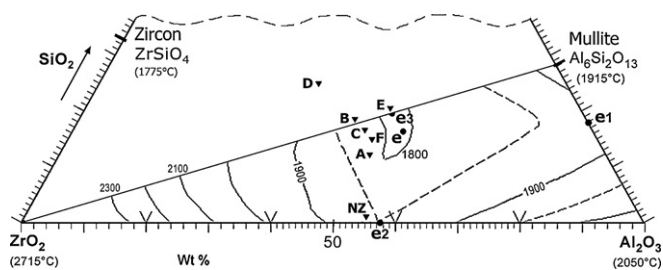


Fig. 1. Part of ternary equilibrium phase diagram showing different compositions of materials used in this study (marked by triangles). Concentration values shown in Table 1 were normalized to 100% with respect to the three main compounds to facilitate plotting in the ternary diagram. Circles denote binary (e1–e3) and ternary (e) eutectic points. Diagram taken from ACerS-NIST Phase Equilibria Diagram, CD-ROM Database, Version 3.0.

The other materials are based on the bulk cast ceramic material called EucorTM.¹² All of the selected materials in powder form were plasma sprayed in air at atmospheric pressure using the water stabilized plasma torch WSP[®] 500. In the plasma spraying process, powder particles (60–100 μm) are injected into a high temperature plasma jet generated by the plasma torch. Individual particles are quickly melted by the plasma and propelled onto a substrate where they spread upon impact and rapidly solidify due to very high heat extraction by the cold substrate. The solidified discs are called splats and they represent the basic building blocks of a coating. Repetitive passing of the plasma torch over a substrate produced coatings from 0.5 mm to several millimeters thick. Further details of the amorphous material preparation by plasma spraying can be found elsewhere.¹¹

Microstructure was characterized by a variety of experimental techniques, namely scanning electron microscopy (SEM), energy dispersive X-ray spectrometry (EDS), transmission electron microscopy (TEM) at 200 kV, and high-resolution TEM (HRTEM) at 300 kV equipped with EDS. Thin foil cross-sectional samples for TEM were prepared either by the wedge-polishing technique¹³ or by crushing into very fine particles using a tungsten carbide mortar and pestle. X-ray diffraction (XRD) was used to determine crystallinity and phase content of the bulk samples and line-profile analysis was employed to estimate crystallite size.

Crystallization behavior was investigated by differential scanning calorimetry (DSC). The DSC experiments were performed using the Setaram SETSYS instrument with a DSC measuring head. Eighty-six milligrams of the finely crushed samples were weighed (± 2 mg) into a 100 μl corundum cru-

cible. Crystallized material of the same composition from the previous runs was used in the reference crucible to obtain a heat capacity of the reference comparable to that of the sample. Pure argon was passed through the measuring head at a constant flow rate. The temperature and heat flow measurements were calibrated by measuring the melting temperature and heat of melting of pure silver and indium. The DSC experiments started by a fast heating (30 K/min) to a temperature of about 100 °C lower than the onset temperature of the crystallization process; then the desired heating rate (1, 2 and 5 K/min, in some experiments also 10 K/min) was applied. After the baseline correction, the net heat release rate due to crystallization as a function of time was obtained and the total crystallization heat evolved was determined by integration. The experimental values of α , mass fraction of material crystallized, were obtained as a ratio of the heat evolved up to a time t and the total heat evolved. Similarly, the normalized crystallization rate $d\alpha/dt$ was calculated as the instantaneous heat release rate divided by the total heat evolved.

3. Results and discussion

3.1. Microstructure of amorphous materials

The microstructure of as-sprayed samples of all investigated materials exhibits a pattern typical for plasma spraying (Fig. 2). Most of the sample consists of thin splats (thin disk-shape lamellae) with a few partially melted particles and cracks. Each splat has a different chemical composition (Fig. 2) due to different proportions of Al and Zr oxides in the individual powder particles. Such chemical variations among splats are present in all as-sprayed materials. Chemical compositions of the powder particles and therefore of the resulting splats vary around the average composition of the two main constituents (Table 1) by as much as ± 10 wt.%. Most of the individual splats in the as-sprayed materials are, however, a chemically homogeneous blend of Al, Zr and Si oxides. EDS line scans were performed in HRTEM within individual splats using electron beam probe size of 5 nm. At the 5 nm resolution, there are no detectable chemical gradients within the splats (Fig. 3a). XRD analysis (Fig. 4) established the as-sprayed samples of Eucor materials to be mainly amorphous with relative amorphous content between 82% and 94% whereas XRD pattern of the as-sprayed NZ material does contain wide peaks of tetragonal zirconia and delta alumina in addition to the amorphous background (relative amorphous content approximately 65%). It was confirmed by TEM that the as-sprayed NZ material contains nanocrystalline regions of tetragonal zirconia and delta alumina, whereas the Eucor materials have most of the splats amorphous. The presence of silica in the sprayed materials (all variants of Eucor) suppresses crystallization during rapid solidification. The crystalline peaks (mainly monoclinic ZrO_2) in Eucor as-sprayed materials come from the embedded partially melted particles. Therefore, the limited crystalline content of the as-sprayed Eucor samples is not related to the chemical composition of individual materials but it is a result of the imperfect nature of plasma spraying processes, which allows a small fraction of the feedstock powder particles to reach the coating only partially melted.

Table 1
Composition of investigated materials in wt.% as determined by energy dispersive X-ray fluorescence.

Material	Al_2O_3	ZrO_2	SiO_2	Other oxides
NZ	52.8	42.7	1.0	3.5
Eucor-A	48.0	36.7	11.6	3.7
Eucor-B	41.9	35.4	17.3	5.4
Eucor-C	44.3	34.9	15.5	5.3
Eucor-D	33.6	38.2	23.7	4.5
Eucor-E	47.2	29.6	19.5	3.7
Eucor-F	46.7	34.8	14.1	4.4

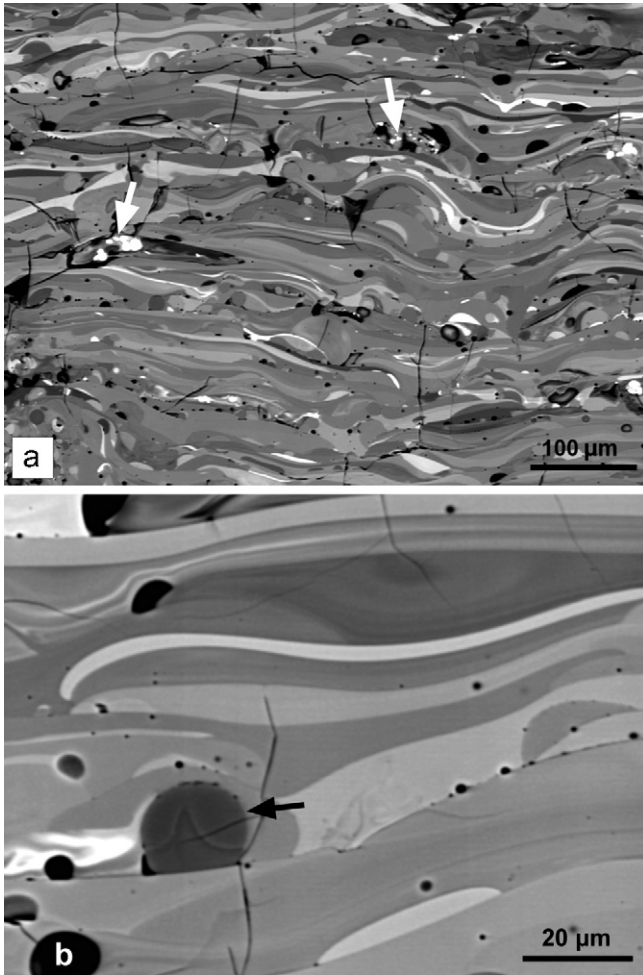


Fig. 2. SEM image (backscattered electrons) of un-etched polished cross-section of as-sprayed samples. Arrows point to partially melted particles: (a) NZ and (b) Eucor-B.

3.2. DSC results

All investigated materials exhibit an exothermic DSC peak upon heating between 940 and 990 °C. As an example, DSC traces of Eucor-F samples for different heating rates are given in Fig. 5. The DSC signals also show a local maximum at a temperature interval of 420–500 °C corresponding to the glass transition (inset in Fig. 5). The exothermic peaks above 900 °C correspond to crystallization of the amorphous material. Most of the DSC peaks exhibit a small irregularity (a shoulder) on one side of the curve due to overlap of the major peak with another small peak. The shoulder may be indicative of a separate crystallization process with only a small contribution to total release of heat (Fig. 6). The heat of crystallization values per unit mass of sample are given in Table 2. These values correlate with the relative amorphous content in the as-sprayed samples estimated from XRD patterns. The lowest heat of crystallization per gram is exhibited by the NZ material, which has the lowest amorphous content in the as-sprayed condition. If the heat of crystallization values are normalized to 100% of amorphous content, a value of 166 ± 5 kJ/kg is obtained for all Eucor materials and 139 kJ/kg for the NZ material.

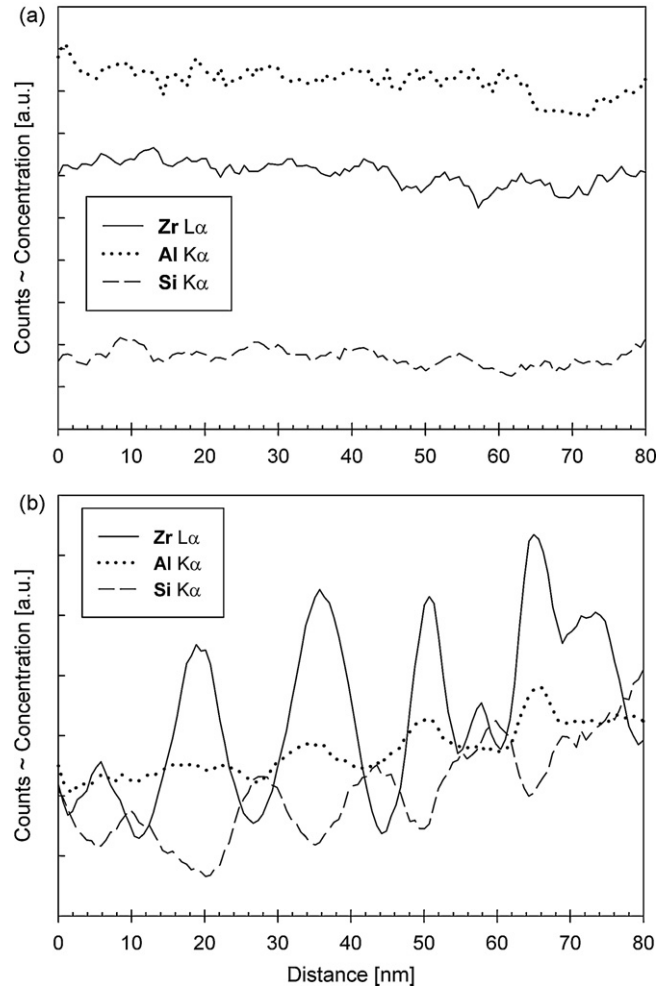


Fig. 3. Examples of EDS line scan analyses performed in HRTEM using a 5 nm probe size: (a) within an amorphous splat and (b) within a nanocrystalline splat.

3.3. Phase content and microstructure of crystallized materials

Samples of all investigated materials were heat-treated to 1000 °C (i.e. above the end of crystallization temperature) in order to study their microstructure and phase content. XRD patterns (Fig. 4) of all the heat-treated samples contain wide peaks of tetragonal ZrO_2 ($t\text{-ZrO}_2$) as the predominant phase and also small, wide peaks of tetragonal $\delta\text{-Al}_2\text{O}_3$. Due to the chemical

Table 2

Heat of crystallization and kinetic characteristics obtained from the DSC measurements.

Material	Heat of crystallization (average value) (kJ/kg)	Activation energy, Kissinger's method (Eq. (3)) (kJ/mol)	Avrami exponent (Eq. (5)) (–)
NZ	88	1349	3.3
Eucor-A	148	1090	1.8
Eucor-B	138	996	1.8
Eucor-C	137	941	2.1
Eucor-D	125	903	1.5
Eucor-E	145	843	2.0
Eucor-F	140	937	2.1

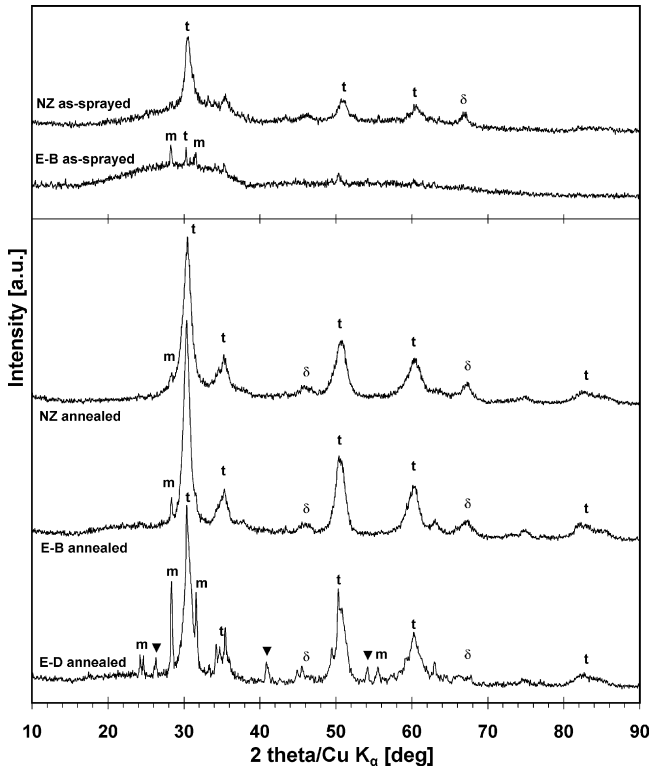


Fig. 4. XRD patterns of selected as-sprayed and annealed samples; t – tetragonal ZrO_2 , m – monoclinic ZrO_2 , δ – delta Al_2O_3 , ▼ – mullite.

differences among individual splats, there is always a certain number of Al-rich splats in all of the investigated materials that crystallize as δ - Al_2O_3 phase nanocrystallites. Crystallization of δ - Al_2O_3 phase is probably responsible for the observed irregularities in DSC peaks. In most of the splats, however, nanocrystallites of alumina–zirconia solid solution are formed with the tetragonal zirconia crystal lattice. The high fraction of Al_2O_3 in t- ZrO_2 solid solution leads to the observed systematic shift

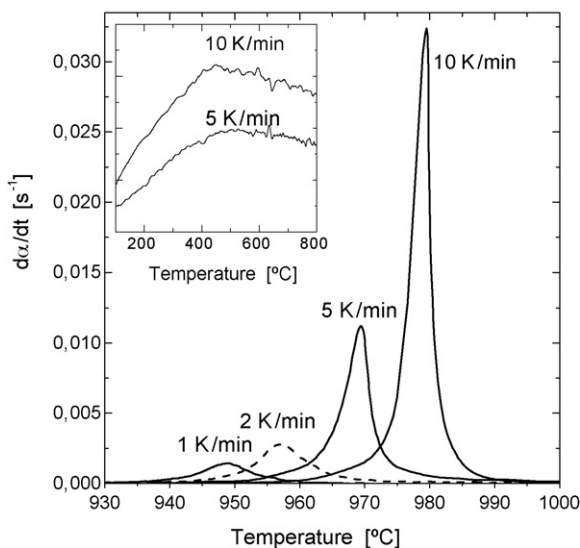


Fig. 5. Heat flow due to crystallization of Eucor-F at different heating rates of 1, 2, 5 and 10 K/min. The inset shows DSC traces (before baseline correction) near the glass transition temperature.

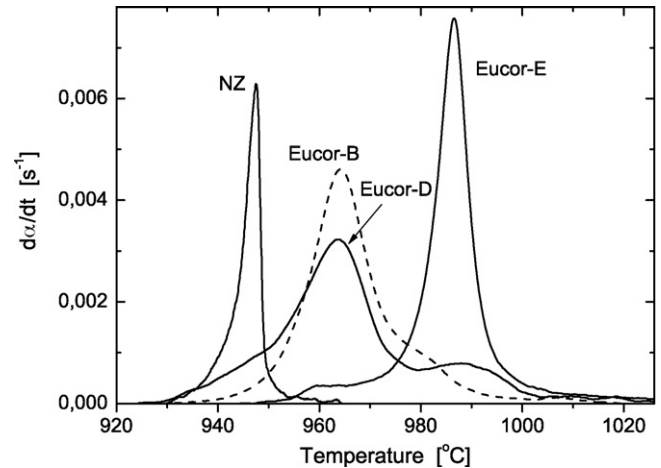


Fig. 6. Comparison of various shapes of DSC traces taken at the heating rate of 5 K/min (Eucor-B, Eucor-D and Eucor-E) and 2 K/min (NZ).

of the diffraction peaks toward higher angles. Radius of the Al atom is smaller than that of Zr atom and thus the tetragonal lattice shrinks when Zr atoms are substituted by Al atoms and hence the d-spacing decreases. The heat-treated Eucor-D material, which has the highest content of silica, is the only material that contains additional small amount of mullite ($3Al_2O_3 \cdot 2SiO_2$) phase (Fig. 4). The presence of mullite can be related to the extra peak showing only in the DSC traces of Eucor-D material (Fig. 6).

Observation of the annealed microstructure was carried out in TEM and HRTEM (Fig. 7). Several hundreds of nanocrystallites were analyzed on several TEM micrographs (e.g. Fig. 7). The TEM results are in good agreement with the XRD line width analysis and the average crystallite size is increasing with increasing silica content from 10.5 nm for NZ material (almost no silica content) to 25 nm for Eucor-D with the highest silica content. The nanocrystallites are approximately spherical (i.e. three-dimensional) and do not form standard angular grain boundaries. There is a fine network of a weak contrast phase in between the individual t- ZrO_2 crystallites that is observed in bright field TEM images (Fig. 7) of all Eucor materials. The fine network surrounding individual crystallites is shown to be an amorphous phase in HRTEM (Fig. 7). The predominant t- ZrO_2 crystallites within each splat are embedded in remains of the original amorphous matrix. EDS line analyses in HRTEM (5 nm probe size) showed that each nanocrystallite is rich in Zr oxide whereas the amorphous matrix is enriched by Si oxide and contains only a small amount of Zr oxide (Fig. 3b). Thus the crystallization in all Eucor materials requires solid-state demixing of ZrO_2 and SiO_2 constituents. The Al oxide content variations (Fig. 3b) follow to a small degree the Zr oxide content. Therefore, the tetragonal zirconia lattice accommodates a high fraction of Al_2O_3 in an extended solid solution. There is no diffusional demixing taking place in the NZ material as there is almost no silica present.

3.4. Kinetic parameters of crystallization

In a DSC crystallization experiment with a linear temperature increase (heating rate $\beta = dT/dt = \text{constant}$), the fractional

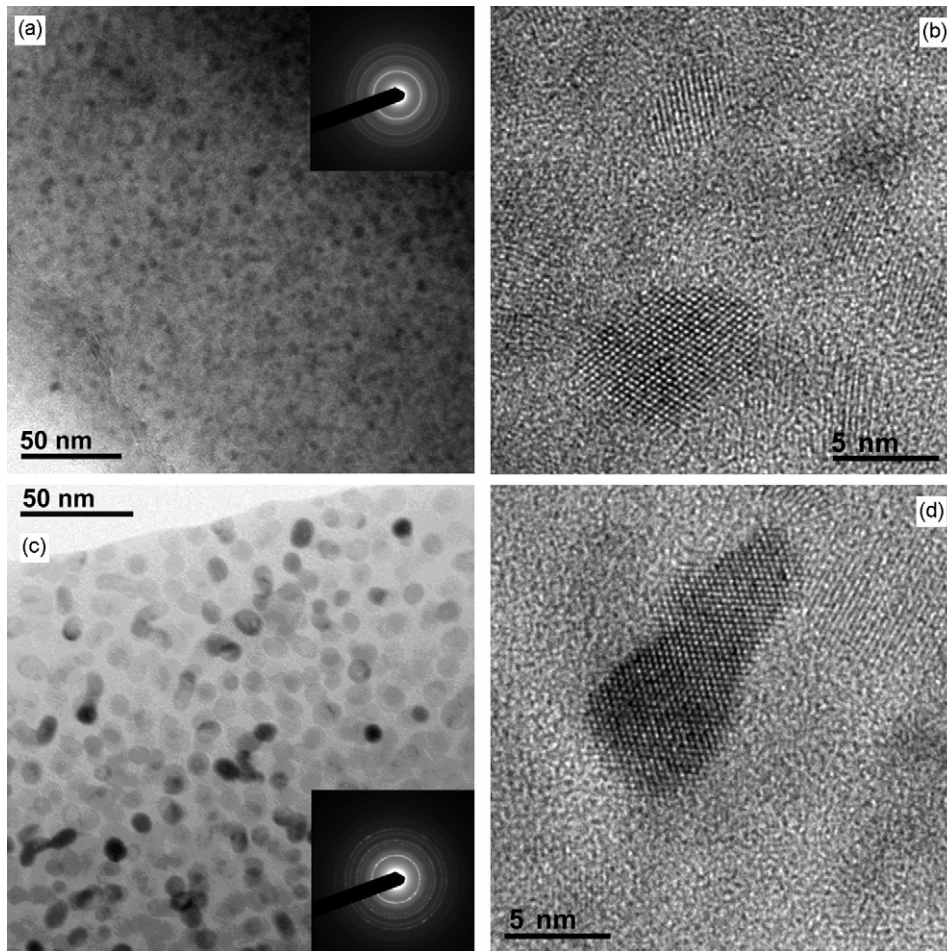


Fig. 7. Bright field TEM and HRTEM micrographs of annealed samples with corresponding diffraction patterns shown as insets: (a) and (b) NZ, (c) and (d) Eucor-A. High-resolution images (b) and (d) show tetragonal ZrO_2 nanocrystals.

conversion α at temperature T is obtained from the measured heat release rate Φ :

$$\alpha = \frac{1}{\beta Q_c} \int_{T_0}^T \Phi \, dT \quad (1)$$

In Eq. (1), Q_c is the total crystallization heat evolved and T_0 is the temperature corresponding to the beginning of crystallization. A general expression for the normalized rate of the crystallization process, $d\alpha/dt$, is written as

$$\frac{d\alpha}{dt} = \frac{\Phi}{Q_c} = \frac{k(T)f(\alpha)}{Q_c} = \frac{k_0 f(\alpha)}{Q_c} \exp\left(-\frac{E_a}{RT}\right) \quad (2)$$

assuming that the crystallization rate is a product of an α -dependent function $f(\alpha)$ and a rate constant $k(T)$ having an Arrhenian temperature dependence; E_a is the apparent (i.e. including contributions from both nucleation and crystal growth) activation energy of the crystallization process.

From a series of experiments with the same material at different heating rates, the activation energy E_a can be determined

by the Kissinger method¹⁴

$$\ln \frac{\beta}{T_p^2} = -\frac{E_a}{RT_p} + \text{const} \quad (3)$$

where T_p is the peak crystallization temperature. Even though the Kissinger method is of approximate nature and more rigorous methods are available,^{15,16} its utilisation is advantageous in evaluation of DSC traces exhibiting irregularities (as mentioned in Section 3.2) since only peak positions, i.e. well-defined quantities, are taken into account. The values of activation energy obtained by the Kissinger method for the materials investigated are summarized in Table 2. There is an approximately linear correlation between the values of activation energy of crystallization and SiO_2 concentration in the material (Fig. 8).

The relatively high values of activation energy are fully comparable with those reported for crystallization of mullite from glasses.¹⁷ There are no data available on activation energies of Zr^{4+} and Si^{4+} diffusion in the Al_2O_3 – ZrO_2 – SiO_2 ternary system. Cherniak¹⁸ studied Si diffusion in zircon (ZrSiO_4) and determined the activation energy to be around 720 kJ/mol for temperatures above 1350 °C. Cherniak also states that diffusion of Si in zircon is about an order of magnitude faster than diffu-

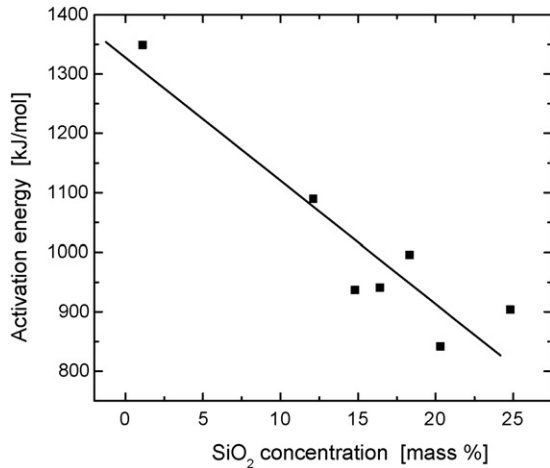


Fig. 8. Plot of apparent activation energies of crystallization against silica concentration.

sion of Hf and many orders of magnitude slower than oxygen diffusion. Hf may be considered as a proxy for Zr, given its similar charge and size, thus the diffusivity of Zr is also smaller than that of Si in zircon¹⁸ and the corresponding activation energy is likely higher. It can be therefore concluded that the measured values of apparent activation energy of crystallization for Eucor materials (from ~900 to ~1100 kJ/mol) are associated with diffusion of Zr ions in the amorphous three-component material. The simultaneous diffusion of Si ions, which is necessary for solid-state demixing of ZrO₂ and SiO₂ leading to crystallization, has probably lower value of activation energy similar to that measured by Cherniak in the case of zircon.

The crystallization processes in amorphous solids are usually interpreted in terms of the standard nucleation and growth kinetic model due to Johnson, Mehl and Avrami (JMA).^{16,19,20} In the JMA model, the relationship for the fractional conversion in a system with a constant heating rate has the form

$$\alpha = 1 - \exp \left[- \left(K(T) \frac{T - T_0}{\beta} \right)^n \right] \quad (4)$$

where n is the Avrami exponent. For a nonisothermal experiment with a constant heating rate, the Avrami exponent may be computed by using Ozawa's method.²¹ Taking twice the logarithm of Eq. (4) gives the relationship:

$$\ln[-\ln(1 - \alpha)] = n \ln[K(T)(T - T_0)] - n \ln \beta \quad (5)$$

Plotting $\ln[-\ln(1 - \alpha)]$ versus $\ln \beta$ for a number of DSC traces taken at different heating rates (where α is obtained at the same temperature) yields the value of n (Fig. 9). The values of the Avrami exponent n for each material investigated are given in Table 2.

The Avrami exponent n can be expressed as $n = a + mb$, where a refers to the nucleation rate with value of 1 for a constant rate, 0 for a zero nucleation rate (site saturation), and $a < 1$ for a decreasing rate, m corresponds to the crystal growth dimensionality, and b relates to the mechanism of growth with the value of 1 for an interface-controlled process and 0.5 for a diffusion-controlled process.²² The Avrami exponent n for the

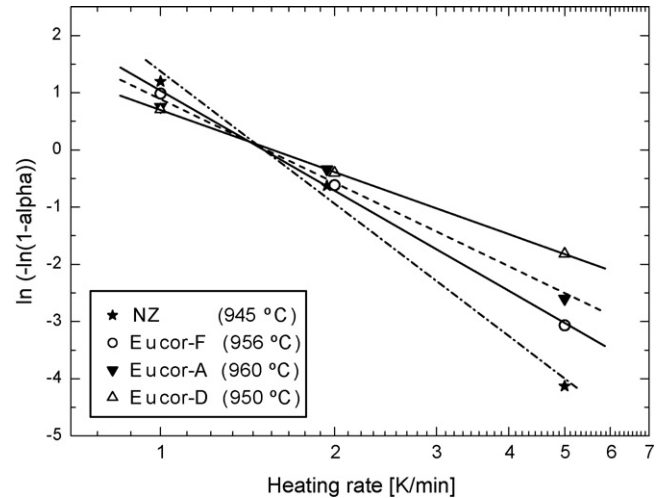


Fig. 9. Plot of $\ln[-\ln(1 - \alpha)]$ against the logarithm of the heating rate for selected materials: NZ, Eucor-A, Eucor-D and Eucor-F (for NZ and Eucor-A at 2 K/min, the data x -coordinates are slightly offset in the plot to improve clarity).

NZ material ($n = 3.3$) stands apart from the n values calculated for the Eucor materials ($1.5 \leq n \leq 2.1$). From the microscopic observations (as described in Section 3.3), it follows that the growth of nanocrystallites in the materials investigated is of the three-dimensional type, $m = 3$. Therefore, the values of the Avrami exponent for ZrO₂ crystallization in the Eucor materials are consistent with a crystal growth mechanism controlled by diffusion transport toward the phase boundary and with instantaneous nucleation. Since the n values for the Eucor materials are on average somewhat higher than the nominal value $n = 1.5$, nucleation of the tetragonal crystallites may to some extent also proceed during the crystal growth process. The Avrami exponent for the NZ material, however, points to a growth mechanism controlled by a reaction at the phase boundary. This is consistent with HRTEM structural observation showing no concentration gradient present in the annealed NZ material.

4. Summary and conclusions

Crystallization kinetics of amorphous alumina–zirconia–silica ceramics was studied for seven different material compositions. The amorphous materials were prepared by plasma spraying thus the sample consists of thin splats (thin disk-shape lamellae) with a significant chemical variation among them due to different proportions of Al and Zr oxides in the individual powder particles. Most of the individual amorphous splats in the as-sprayed materials are chemically homogeneous.

The amorphous materials crystallize above 920 °C primarily as tetragonal ZrO₂ solid solution with Al₂O₃ and to a small extent as δ -Al₂O₃ in Al₂O₃-rich splats. The tetragonal zirconia nanocrystallites have average diameters increasing from 10.5 to 23 nm with increasing silica content. For silica-containing materials the nanocrystallites are embedded in silica rich remains of the amorphous matrix thus creating steep concentration gradients at the nanocrystal/glass interface. The kinetic stabilization of the nanoscale microstructure is related to the silica rejection

during growth involving a soft impingement between neighboring nanocrystallites.

The apparent activation energy of the crystallization increases approximately from 850 to 1350 kJ/mol with decreasing silica content. These activation energy values are comparable to those reported for crystallization of mullite from glasses. Based on the values of Avrami coefficient and on the microstructural observations, crystallization mechanism of the silica-containing materials is best described by instantaneous nucleation followed by three-dimensional crystal growth controlled by diffusion transport of Zr and Si cations in opposite directions (demixing). The Avrami exponent for the NZ material, however, points to a three-dimensional growth mechanism controlled by a reaction at the phase boundary.

Acknowledgments

This work was supported by Project No. KAN300430651 carried out under the “Nanotechnologies for Society” program administered by the Academy of Sciences of the Czech Republic. Further funding was based on Institutional Research Plans No. AV0Z40320502 and No. AV0Z20430508 of the Institute of Inorganic Chemistry AS CR and the Institute of Plasma Physics AS CR, respectively.

References

1. Winterer, M., *Nanocrystalline Ceramics: Synthesis and Structure*. Springer Series in Materials Science, vol. 53. Springer, Berlin/New York, 2002, pp. 228–232.
2. Kear, B. H., Colaizzi, J., Mayo, W. E. and Liao, S. C., On the processing of nanocrystalline and nanocomposite ceramics. *Scripta Mater.*, 2001, **44**, 2065–2068.
3. Duan, R.-G., Zhan, G.-D., Kuntz, J. D., Kear, B. H. and Mukherjee, A. K., Spark plasma sintering (SPS) consolidated ceramic composites from plasma-sprayed metastable Al_2TiO_5 powder and nano- Al_2O_3 , TiO_2 , and MgO powders. *Mater. Sci. Eng. A*, 2004, **373**, 180–186.
4. Pawlowski, L., Finely grained nanometric and submicrometric coatings by thermal spraying: a review. *Surf. Coat. Technol.*, 2008, **202**, 4318–4328.
5. Wu, R. I., Wilde, G. and Perepezko, J. H., Glass formation and primary nanocrystallization in Al-base metallic glasses. *Mater. Sci. Eng. A*, 2001, **301**, 12–17.
6. Pawlowski, A., Morgiel, J. and Czeppe, T., Amorphisation and crystallisation of phases in plasma sprayed Al_2O_3 and ZrO_2 based ceramics. *Arch. Metall. Mater.*, 2007, **52**, 635–639.
7. Kim, H. J. and Kim, Y. J., Amorphous phase formation of the pseudo-binary Al_2O_3 - ZrO_2 alloy during plasma spray processing. *J. Mater. Sci.*, 1999, **34**, 29–33.
8. Zhou, X. Z., Shukla, V., Cannon, W. R. and Kear, B. H., Metastable phase formation in plasma-sprayed ZrO_2 (Y_2O_3)- Al_2O_3 . *J. Am. Ceram. Soc.*, 2003, **86**, 1415–1420.
9. Petersson, A., Keshavan, H. and Cannon, W. R., Nanostructured ceramics processed from coarse powder. *Mater. Sci. Eng. A*, 2008, **475**, 62–67.
10. Vasiliev, A. L., Padture, N. P. and Ma, X. Q., Coatings of metastable ceramics deposited by solution-precursor plasma spray. I. Binary ZrO_2 - Al_2O_3 system. *Acta Mater.*, 2006, **54**, 4913–4920.
11. Chráska, T., Neufuss, K., Dubsy, J., Ctibor, P. and Klementova, M., Fabrication of bulk nanocrystalline ceramic materials. *J. Therm. Spray Technol.*, 2008, **17**, 872–877.
12. Eutit Ltd., www.eutit.cz.
13. Chráska, T., Transmission electron microscopy of plasma sprayed ceramic deposits. *Acta Tech. CSAV*, 2006, **51**, 403–413.
14. Kissinger, H. E., Reaction kinetics in differential thermal analysis. *Anal. Chem.*, 1957, **29**, 1702–1706.
15. Yinnon, H. and Uhlmann, D. R., Applications of thermoanalytical techniques to the study of crystallization kinetics in glass-forming liquids. Part I. Theory. *J. Non-Cryst. Solids*, 1983, **54**, 253–275.
16. Kasap, S. O. and Juhasz, C., Theory of thermal analysis of non-isothermal crystallization kinetics of amorphous solids. *J. Chem. Soc., Faraday Trans. 2*, 1985, **81**, 811–831.
17. Okada, K., Activation energy of mullitization from various starting materials. *J. Eur. Ceram. Soc.*, 2008, **28**, 377–382.
18. Cherniak, D., Si diffusion in zircon. *Phys. Chem. Miner.*, 2008, **35**, 179–187.
19. Kempen, A. T. W., Sommer, F. and Mittemeijer, E. J., Determination and interpretation of isothermal and non-isothermal transformation kinetics; the effective activation energies in terms of nucleation and growth. *J. Mater. Sci.*, 2002, **37**, 1321–1332.
20. Malek, J., Kinetic analysis of crystallization processes in amorphous materials. *Thermochim. Acta*, 2000, **355**, 239–253.
21. Ozawa, T., Kinetics of non-isothermal crystallization. *Polymer*, 1971, **12**, 150–158.
22. Sung, Y. M., Nonisothermal phase formation kinetics in sol-gel-derived strontium bismuth tantalate. *J. Mater. Res.*, 2001, **16**, 2039–2044.